Probe shape measurement in an electron beam lithography system

J. Alexander Liddle[a)]
Center for X-Ray Optics, Lawrence Berkeley National Laboratory, Mail Stop 2-400, 1 Cyclotron Road, Berkeley, Calfornia 94720-8232
Molecular Foundry, Lawrence Berkeley National Laboratory, Mail Stop 2-400, 1 Cyclotron Road, Berkeley, California 94720-8232

Patrick Naulleau
Center for X-Ray Optics, Lawrence Berkeley National Laboratory, Mail Stop 2-400, 1 Cyclotron Road, Berkeley, Calfornia 94720-8232

Gerard Schmid
Molecular Foundry, Lawrence Berkeley National Laboratory, Mail Stop 2-400, 1 Cyclotron Road, Berkeley, California 94720-8232

We have devised a method of quantifying the size and shape of the probe in a Gaussian-beam lithography system. The technique is robust, being insensitive to noise, but is sensitive to changes in the probe size of as little as ±0.5 nm. We have determined that the probe shape of our system is indeed well fit by a Gaussian, with a best-focus full-width half-maximum of 6.5±1 nm. We are able readily to quantify the effects of astigmatism on the system. In addition, the approach we describe can be extended to deal with arbitrary point-spread functions. © 2004 American Vacuum Society. [DOI: 10.1116/1.1821579]

INTRODUCTION

Characterizing the probe in scanning probe instruments accurately is essential in order to understand their performance, but it is generally extremely difficult to do so. In particular, in electron beam lithography tools, it is desirable to know not only the probe size, but also the details of the probe shape. If the probe shape is known, it is then possible to begin separating the various effects that contribute to the resolution limit of the system: probe shape, energy deposition distribution, resist chemical changes, and development processes. In practical terms, a known probe shape would permit the development of a more effective interproximity effect correction algorithm, which should improve the process latitude for very small features.

The most commonly used technique for spot size measurement in Gaussian beam lithography tools is the knife-edge scan.[1] This approach has numerous potential sources of error, such as edge sharpness, contamination, and electron scattering in the sample. More robust techniques rely on Fourier methods, such as those proposed by Zhang *et al.*[2] and Joy,[3] but these do not yield a measure of the spot shape unless assumptions about the spatial frequency distribution are made (e.g., it is white). They are also unable to detect asymmetry in the point-spread function (PSF) because they rely on estimates of the probe spatial power spectrum.

In this article we describe a probe shape measurement technique that we have implemented on our electron beam lithography system. We also present results obtained with this method and discuss the advantages and disadvantages of our technique as compared with others.

PROBE-SHAPE MEASUREMENT METHOD

In principle, a probe's shape can be determined by imaging a perfectly known test sample with that probe and then using a deconvolution process on the resulting image. Unfortunately, since we are typically always at the limit of resolution, it is almost impossible to find a method of characterizing the test sample that operates with the same contrast mechanism as that of the probe under investigation. This means that there will always be difficulties in interpreting the relationship between the test sample and the image generated by the probe. Consider, for example, scanning electron microscope and atomic-force microscope images of a sample: Both contain a variety of imaging artifacts[4,5] that cannot be unambiguously interpreted and cross correlated if the sample is not known beforehand.

In the case of an electron beam lithography tool, however, the minimum probe size is determined by balancing resolution against beam current in order to obtain adequate throughput. The probe size is thus far larger than would be typical of system designed for imaging and we therefore have an opportunity to produce an almost ideal test sample.

We have taken advantage of the presence in our lithography system[6] of a transmission detector to take bright-field scattering-contrast[7] images at a 100 keV beam energy of a sample of Au islands approximately 30 nm thick on a 100 nm thick SiN membrane. This sample provides a wide range of feature sizes and generates a high contrast image under these conditions. The beam writer has a minimum scan pixel size of 2 nm.

[a)]Author to whom all correspondence should be addressed: Rm 2-419, Lawrence Berkeley National Lab, 1 Cyclotron Road, Berkeley, CA 94720; electronic mail: jaliddle@lbl.gov
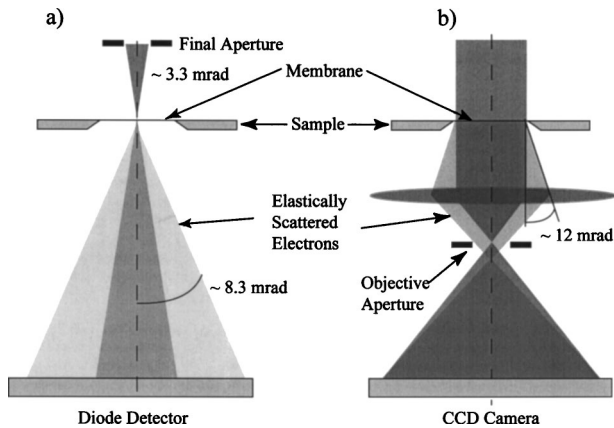
FIG. 1. Detector geometries in the beamwriter (a) and the TEM (b). The acceptance angles of the diode detector (beam writer) and the objective aperture (TEM) determine the details of the image contrast.

Images of the same sample were also taken in a transmission electron microscope (TEM) at the same electron energy and with a comparable detector geometry (Fig. 1). The resolution in the TEM under the conditions used was approximately 0.57 nm—far higher than that of the beam writer. The TEM images thus serve as the known object function.

We note that, even though the identical sample is used in both systems, subtle differences in contrast can arise from variations in detector linearity and from differences in detector geometry. We have determined the importance of the latter effect by calculating the contrast versus Au thickness of the two systems (Fig. 2), which shows that there is, at the most, a 2% difference between the two. The maximum thickness of the Au islands was measured by atomic force microscopy to be 30 nm. At small thicknesses there is very little difference in transmission since very thin films will scatter few electrons outside the detector acceptance angle. At large thicknesses there is very little difference because thick films scatter essentially all the incident electrons outside the detector acceptance angle. In the following discussion we have assumed that difference is small enough not to require compensation and the results are calculated accordingly.
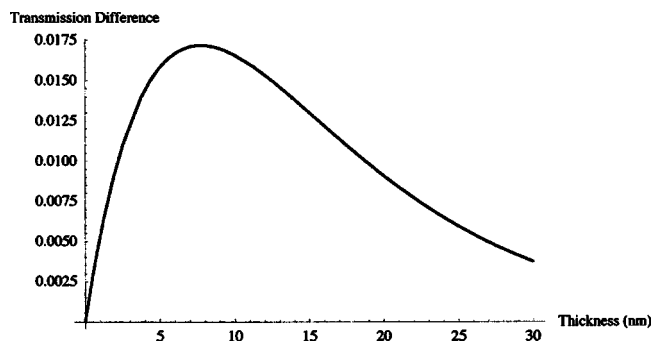

FIG. 2. Calculated difference in transmission as a function of thickness for a Au film for the relevant detector acceptance angles for the beamwriter (8.3 mrad) and the TEM (12 mrad). The maximum difference is <2%.
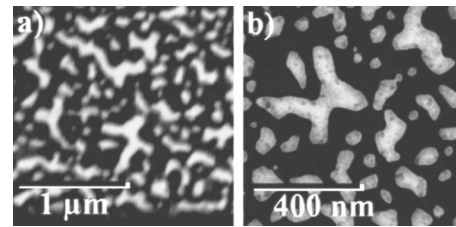

FIG. 3. (a) Measured (beamwriter image) distribution of the same area and (b) known object distribution (TEM image of Au island sample).

FITTING ALGORITHM

The PSF fitting algorithm relies on starting with a known object distribution (TEM image) and estimating the PSF by comparing the theoretical image distribution (calculated from the estimated PSF and object distributions) to the measured distribution (beamwriter image). Figure 3 shows representative measured (beam-writer image) and known (TEM image) distributions.

The first step in the process is to perform a coarse alignment between the images using a set of manually selected matching control points in the two images. This coarse alignment corrects magnification, rotation, and offset. The coarse alignment is then followed by correlation-based fine alignment steps to refine the alignment to the subpixel level.[8] In all cases it is the TEM image that is manipulated to coincide with the exposure tool image. We have chosen this approach because of the higher resolution and signal-to-noise ratio of the TEM image. As noted above, the TEM image has a pixel size of 0.57 nm, whereas the exposure tool image has a pixel size of 2 nm. Once manipulated, however, the TEM image is forced to a pixel size of 2 nm matching that of the exposure tool image. Figure 4 shows the aligned images corresponding to the source images from Fig. 3.

The next step in the process is to perform the actual fit of the PSF. This involves the use of a nonlinear least-squares routine where the error function is the difference between the theoretical image distribution and the measured (beamwriter) image distribution. In the results presented here, the PSF has been functionally described as a Gaussian with variable major and minor axis standard deviations and variable orientation. We note that we have also tried a combination of Gaussian and Lorentzian functions, but have determined that the Lorentzian component is so small that is probably not statistically significant and have therefore chosen to use only
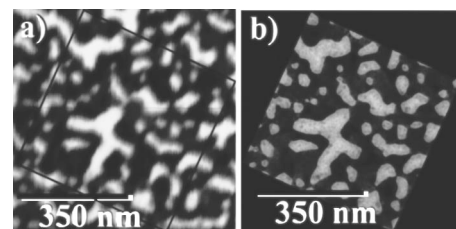

FIG. 4. (a) Measured (beamwriter image) distribution of Au island sample and (b) known object distribution (TEM image) of the same area after scaling and rotation corrections have been applied.
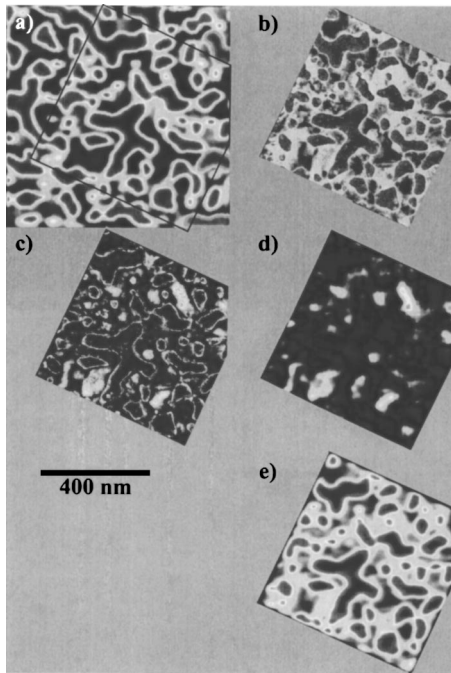
FIG. 5. Steps in the PSF fitting process. (a) Reference image from beam-writer with bounding box indicated, (b) object image from TEM, after scaling and rotation matching, (c) difference image (note the large signal from the feature edges), (d) difference image after the final (154th) iteration (note the signal from the feature edges has almost disappeared, and (e) final fitted image.

the Gaussian representation. Because the modeled image formation process is incoherent, the PSF is represented as a pure amplitude function. Moreover, this incoherent imaging condition means that it is sufficient to know only the amplitude distribution of the object. If this were not the case, we would not be able to use the TEM image as a valid representation of the object as it does not include phase information. The theoretical image is calculated through a convolution process between the iteration-dependent estimated PSF and the known object. Figure 5 shows steps in the fitting process: The mismatch between the images at the feature edges decreases dramatically as the fit becomes better. The figure also shows that there are areas where the two images do not match at all (a consequence of diffraction effects in the TEM), but these are effectively ignored by the least-squares fitting algorithm. Such areas can also be forced to be explicitly ignored by the algorithm by applying a mask to the error function.

Finally, it is important to note that this method could be further generalized by removing the requirement that there be a functional description of the PSF and using instead a pixel-based description. The drawback with this approach is that the number of fitting variables increases dramatically because now every pixel of the PSF is an independent variable. Representing the PSF as a 20×20 pixel array would yield a total of 400 independent variables. Nevertheless, this approach is feasible with modern computers and optimization techniques and has the potential to reveal asymmetries in the PSFs.
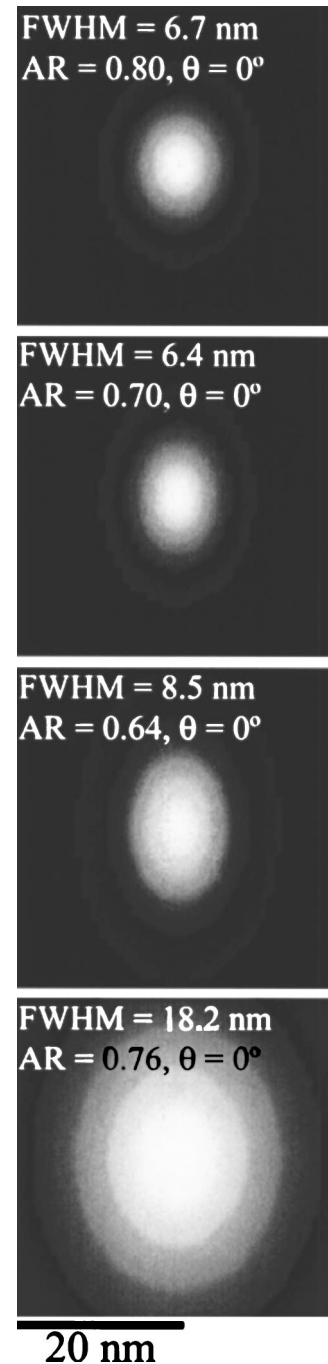

FIG. 6. Through-focus images showing variation in PSF as a function of defocus. The full-width half-maximum (FWHM) and aspect ratio (AR) and orientation of each PSF are indicated. The FWHM is measured across the minor axis. An orientation of 0° corresponds to the major axis being vertical. The axes' scales are nanometers. The defocus values are 1.9, 3.3, 6.0, and 10.0 μm, respectively, from top to bottom.

RESULTS

Figure 6 shows the results of using the fitting algorithm on a through-focus sequence of images after using the automated focus and stigmation algorithm. There is a noticeable ellipticity in the probe shape even at the nominal best focus. As focus is adjusted the probe aspect ratio remains relatively constant but, as expected, the size of the probe increases.
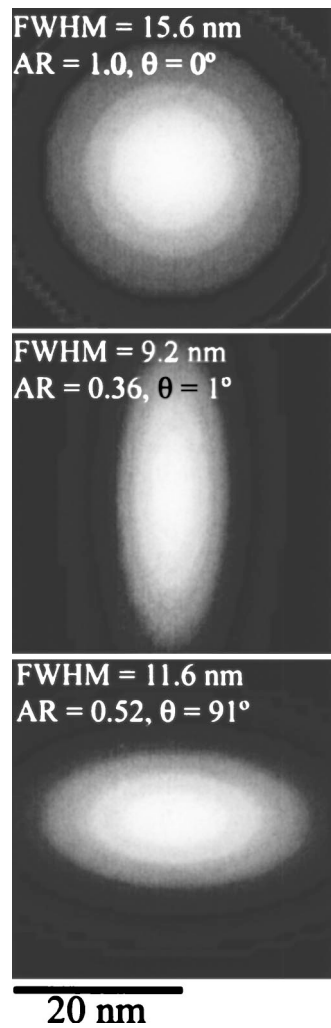
FIG. 7. Through-focus images showing variation in PSF for a fixed amount of astigmatism. The full-width half-maximum (FWHM) and aspect ratio (AR) and orientation of each PSF are indicated. The FWHM is measured across the minor axis. An orientation of 0° corresponds to the major axis being vertical. The axes scales are nm.

Figure 7 illustrates the effect of introducing a fixed perturbation in one of the stigmators and varying focus (the complete data are given in Table I). At the nominal best focus the PSF is large, but symmetrical. This point is referred

TABLE I. Values for PSF full-width half-maximum (FWHM), aspect ratio (AR), and orientation for a series of different defocus values with a constant astigmatism setting.

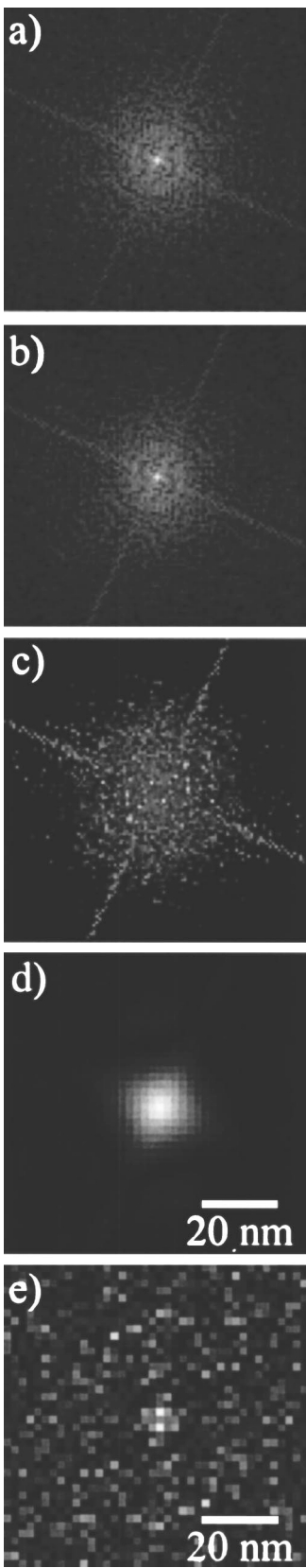| Defocus (μm)	FWHM (minor axis)	Aspect ratio	Angle
0.0	15.6	1	NA
−1.8	11.6	0.52	91
0.0	16	1.1	28
1.8	12.4	0.64	−1
3.6	9.2	0.36	1
5.5	8	0.27	1
7.3	9.5	0.26	0
9.1	10.6	0.27	0

FIG. 8. Analytic calculation of the PSF for the last image in Fig. 7 (FWHM 11.6 nm, AR=0.52, θ=91°). (a) Logarithmically scaled object (TEM) spectrum, (b) logarithmically scaled transformed (beamwriter) spectrum, (c) transfer function, (d) recovered PSF, and (e) PSF recovered without thresholding.

to as the circle of least confusion. As we scan the through focus, the aspect ratio changes to give a typical astigmatic probe shape. Note that because we have kept the stigmators fixed and varied only the focus in the presence of the stigmator error the orientation of the PSF does not change until we go through focus, at which point it jumps 90°. The intermediate angles seen in Table I are a manifestation of the measurement limits. Based on repeated measurements at the circle of least confusion we find the precision of the measurement to be approximately ±1 nm peak-to-valley.

DISCUSSION

Because we are using an object that is effectively known, we could, in principle, extract the PSD analytically instead of using a numerical estimation technique. In a linear system, as we have assumed here, the spectrum of the image is simply the spectrum of the object times the transfer function of the system. The system transfer function, from which we can compute the PSD through a Fourier transform, can thus be recovered by dividing the image spectrum by the object spectrum. The problem with using this approach in practice, however, is that it is extremely sensitive to noise as well as numerical problems related to dividing by extremely small numbers. The numerical division problem can be mitigated by ignoring all points falling below some chosen threshold in the object spectrum, but the noise problem is not so easily dealt with. Moreover, thresholding is invariably a source of artifacts as a result of the artificially sharp cutoffs it imposes in the spectral domain.

Figure 8 shows results obtained using the analytical approach. In this example we use the images corresponding to the second focus setting for the astigmatic case described above. Before calculating the relevant spectra, care must still be taken to properly prealign the images in magnification and rotation as described above. The logarithmically scaled object (TEM) and image (beam-writer) spectra are shown in Figs. 8(a) and 8(b), respectively. The calculated transfer function and PSF are shown in Figs. 8(c) and 8(d), respectively. The recovered PSF suffers from artifacts related to the spatial domain mask used to select overlapping regions in the image and object distributions as well as simply providing a grossly inaccurate representation of the PSF, which should be about 23 and 12 nm wide along the major and minor axes, respectively, with the major axis running in the horizontal direction. For the sake of completeness, the PSF results ob-

tained without the use of thresholding is shown in Fig. 8(e). Again, the resulting PSF is observed to be meaningless.

It should be pointed out that the Fourier techniques described by Zhang et al.[2] and Joy[3] are extremely useful for tracking system performance by providing methods of making quantitative comparisons of the state of the tool over time and are relatively simple and quick to implement. Our approach is more time consuming, but does yield absolute measures of probe size *and* shape.

CONCLUSIONS

We have presented details of a probe-shape measurement technique, including the algorithm, together with a discussion of those factors, such as detector geometry and linearity, which can influence the accuracy of the results. We have presented a set of measurements obtained on our system that illustrate the utility of this method. We have also described how the approach can be extended to completely arbitrary PSFs. The results will provide input into interproximity effect models and assist in the deconvolution of aerial image, deposited energy, and resist development effects on lithographic resolution. The technique has sufficient sensitivity to permit the detailed mapping of electron-optical aberrations in lithography systems that will enable the verification of electron-optical models and aid in system design.

Future work will address the slight mismatch in the TEM and beam-writer images due to the differences in illumination angles and detector aperture sizes in order to improve the ultimate accuracy of the technique.

[1]E. Kratschmer, S. A. Rishton, D. P. Kern, and T. H. P. Chang, J. Vac. Sci. Technol. B **6**, 2074 (1988).
[2]N. F. Zhang, M. T. Postek, R. D. Larrabee, A. E. Vladar, W. J. Keery, and S. N. Jones, Scanning **21**, 246 (1999).
[3]D. C. Joy, J. Microsc. **208**, 24 (2002).
[4]J. E. Griffith and D. A. Grigg, J. Appl. Phys. **74**, R83 (1993).
[5]Ludwig Reimer, *Image Formation in Low-Voltage Scanning Electron Microscopy* (SPIE, Bellingham, 1993).
[6]Leica VB6HR operating at 100 kV.
[7]Ludwig Reimer, *Transmission Electron Microscopy*, 4th ed. (Springer, Berlin, 1997).
[8]For a description of a similar process see E. H. Anderson, D. Ha, and J. A. Liddle, Microelectron. Eng. **73-74**, 74 (2003).